



A unified mathematical modelling and simulation for cathodic blistering mechanism incorporating diffusion and fracture mechanics concepts

M.H. Nazir, Z.A. Khan & K. Stokes

To cite this article: M.H. Nazir, Z.A. Khan & K. Stokes (2015) A unified mathematical modelling and simulation for cathodic blistering mechanism incorporating diffusion and fracture mechanics concepts, Journal of Adhesion Science and Technology, 29:12, 1200-1228, DOI: [10.1080/01694243.2015.1022496](https://doi.org/10.1080/01694243.2015.1022496)

To link to this article: <https://doi.org/10.1080/01694243.2015.1022496>



© 2015 The Author(s). Published by Taylor & Francis.



Published online: 27 Mar 2015.



[Submit your article to this journal](#)



Article views: 1246



[View related articles](#)



[View Crossmark data](#)



Citing articles: 3 [View citing articles](#)

A unified mathematical modelling and simulation for cathodic blistering mechanism incorporating diffusion and fracture mechanics concepts

M.H. Nazir^{a*}, Z.A. Khan^a and K. Stokes^b

^aSustainable Design Research Centre, Faculty of Science and Technology, Bournemouth University, Poole, Dorset BH12 5BB, UK; ^bDefence Science and Technology Laboratory (DSTL), Salisbury, UK

(Received 22 August 2014; accepted 13 February 2015)

A novel mathematical model has been developed to understand the mechanism of blister initiation and propagation. The model employs a two-part theoretical approach encompassing the debondment of a coating film from the substrate, coupled with the design components incorporating diffusion and fracture mechanics, where the latter is derived from equi-biaxial tensile loading. Integrating the two components, a comprehensive mathematical design for the propagation of blister boundaries based on specific toughness functions and mode adjustment parameters has been developed. This approach provided a reliable and efficient prediction method for blister growth rate and mechanisms. The model provided a foundation for holistic design based on diffusion and mechanic components to enable better understanding of the debondment of thin elastic films bonded to a metallic substrate.

Keywords: mathematical modelling; simulation study; paint coatings; fracture mechanics; diffusion laws; delamination; blistering; debonding

Nomenclature

Unless otherwise specified, the following nomenclature is used in this paper:

Notations	Description
T	absolute temperature (K)
R	ideal gas constant ($=8.3145 \text{ JK}^{-1} \text{ mol}^{-1}$)
D_i	diffusion coefficient of species 'i' in aqueous medium (mm^2/s)
D_i^*	diffusion coefficient of species 'i' at the interface of metal/coat (mm^2/s)
N_i	flux of species in dilute electrochemical system ($\text{mol}/\text{mm}^2 \text{ s}$)
N_i^*	flux of species inside the blister cavity at the interface ($\text{mol}/\text{mm}^2 \text{ s}$)
Ω	partial molar volume of diffusing species (mm^3/mol)
μ	chemical potential of diffusing specie (kJ/mol)
c	average concentration of diffusing species (mol/mm^3)
E	Young's modulus of coating (GPa)
ν	Poisson's ratio of coating
F	edge compression (N/mm)
F_c	critical edge compression (N/mm)
H	film micro-hardness (N/mm^2)
σ	equi-biaxial compressional (diffusion induced) stress in the coating (GPa)
σ_c	critical stress (GPa)

*Corresponding author. Email: hnazir@bournemouth.ac.uk

ϵ	normal plane strain
h	thickness of coat (mm)
b	radius of blister (mm)
W_a	average wavelength of abrasion (mm)
R_a	amplitude of substrate surface abrasion or roughness (mm)
ΔL	change in the length of coat (mm)
ξ	dimensionless ratio of linear deflection per unit coating thickness
δ	linear deflection of coat (mm)
M_B	bending moment per unit length (GPa mm ²)
ΔS	resultant stress force per unit length (GPa mm)
G_m	elastic energy stored in the bonded film (GPa mm)
Γ_{IC}	mode I stress intensity factor (GPa mm)/mode I toughness
ψ	dimensionless mixed mode parameter
K_I, K_{II}	mode I and mode II stress intensity factors (GPa mm ^{1/2})
α, β	dimensionless elastic mismatch parameters
$\omega(\alpha)$	angular deflection w.r.t elastic mismatch parameters (°)
Υ and λ	two dimensionless phenomenological roughness parameters

1. Introduction

Cathodic blistering is one of the most severe processes responsible for metal-coating interface degradation [1–3] and remains one of the key issues.[4–6] This form of degradation depends upon similar parameters as for cathodic delamination,[7–26] although it has a slightly different failure mechanism. Blister initiation and growth occur when coated steel plates with incipient defects are exposed to alkaline environments.[27] The time for cathodic blister initiation is relatively longer for defect-free coatings when compared to defect-induced coated surfaces. Mathematical models need to be developed for quantifying the mechanisms of blister initiation and growth to enhance the effectiveness of a protective coating. This research presents a novel analytical technique addressing the aforementioned issues when coated steel plates are subjected to highly alkaline environments.

Protective coatings tend to prevent the effects of physical and chemical attack on the substrate. However, in some circumstances, this attack is promoted, rather than hindered, and results in blister initiation.[28] There are several causes of blister initiation: artificial defects and pores in coatings [29,30] and micro-cracks [31] leading to the substrate. These defects provide channels for water and oxygen to diffuse towards the metal/coating interface. In an alkaline environment, the corrosion process starts with the formation of anodic and cathodic sites within or near the blister area. Anodic sites are formed within the range of salt contamination, while cathodic sites are formed under the blister area and corrosion products are deposited between both anodic and cathodic sites.[28] The anodic sites are developed at coating defects in neutral salt solution environments.[29,32] Irrespective of whether the solution is alkaline or neutral, the cathodic reaction always takes place beneath the coating, while the corrosion products formed serve as a basis for metal coat degradation/debondment.

Once a blister has initiated, it continues to grow, leading to the debondment of the coating from the substrate. The blister growth mechanism is generally believed to be a combination of the osmotic pressure developed due to the cathodic reaction and debondment.[3,4,6,27,28,32] The size of the blister enlarges with increased osmotic pressure as more water diffuses in, causing blister propagation. The increased pressure causes the coating to detach from the substrate once the residual stresses exceed the critical stress level. As the coating detaches, the propagation of the interfacial

debondment is subjected to mixed mode conditions, which depends upon the elastic energy released (G) and dimensionless mixed mode parameter (ψ).

Previously, the Hutchinson model [33–35] was based on a comprehensive study of fracture mechanic concepts defining coating debondment mechanisms. Following this, Nguyen et al. [31] introduced the concept of a semi-double cantilever beam to explain cathodic blistering through a micro-mechanics model. However, in recent research, separate numerical models were developed by Prawoto to simulate the ionic transport and fracture mechanics needed for blister propagation.[6,36,37] A similar blistering model was developed by Prawoto and Onn [38] by combining diffusion concept with fracture mechanics but it did not address the following issues: (i) effect of chemical potential and partial molar volume of diffusing species on diffusion induced stress for the coat, (ii) effect of substrate roughness on fractured interface toughness, (iii) elastic energy release rate, G , as a result of blistering, (iv) influence of mode-adjusted debondment driving force on blister propagation and (v) effect of Dandur's elastic mismatch parameters on debondment problem. Another blistering model developed by Prawoto and Onn [39] provided with an efficient J -integral concept but again it did not include the effects of chemical potential, substrate roughness and elastic mismatch on interfacial toughness. All these issues have been accurately modelled in this paper.

The current research has developed a modified model that provides a foundation for an efficient analytical design incorporating the concepts of both diffusion and fracture mechanics. This paper presents an innovative conceptual and analytical model for blistering initiation and propagation to predict the service life of coating systems. The governing equations within the modified model for both components have been designed independently and then fused to form a governing law for blister propagation based on toughness functions. These functions depend on two roughness parameters and are adapted for a dual-mode (mode 1 and mode 2) approach for analysing interfacial debondment propagation behaviour. The two roughness parameters upon which the toughness function depends are useful both for analysing various levels of blister growth and the toughness of debonding edge interfaces. These interfaces are considered to be tougher in mode 2 rather than mode 1.

The model is founded on experimental data, including all the parameters for blistering. The simulation results have been thoroughly compared with the experimental results and model has been accurately validated and *provides a foundation for future research within the area of coating failure analysis and prediction.*

2. Experimental set-up and observations

2.1. Sample preparation and coating

AISI 1010 carbon steel was used as test sample with dimension 2.5×5 cm. All three samples (SI, SII and SIII) were conditioned through surface preparation using polishing wheels with emery papers of 36, 200 and 600. Surface preparation was followed by deep acetone cleansing. The test samples were applied with thin coatings referred to as primer in this paper. The primer was prepared at a thinning ratio (by volume) of 5:1 (five parts of primer to one part of thinner). Conventional spraying gun with fluid tip size of 1.4 mm was used at a working pressure of 3.5 bar for spraying primer. The spraying viscosity was kept as 45 s ISO Cup at 20 °C. The substrate was dried at 20 °C for 6 h for a thorough dry. The film thickness on each conditioned sample was kept constant within a range of 0.016–0.019 mm.

2.2. Fracture mechanics set-up

The average surface roughness, film thickness and debonded area (blistered area) are measured using three-dimensional (3D) scanning interferometry.[40] Roughness values for the substrate and thickness values of primer film are averaged through 20 data points per sample using 3D surface scanning interferometry. The radii of circular blisters (r) at interface of the coat and substrate were calculated using interferometry which is the arithmetic mean of 20 measurements for each sample. The volume of blisters for thin film has been quantified through surface profiling using interferometry.

Hardness values of the coatings were calculated by deploying a micro-hardness indentation (HM-210 Vickers Hardness Testing) technique. Each sample was subjected to 100 gf (1 N) with a load dwell time of 15 s. Hardness values in (N/mm²) were calculated for each sample and are arithmetic mean of five measurements for each sample.

The stress measurements were performed using extremely sensitive laser-based system for *in situ* monitoring of thin-film stresses.

2.3. Diffusion set-up

Conditioned samples were then kept in sodium chloride (NaCl) solution at 20 °C, 0.65 M (37.98 g) of NaCl dissolved in 11.1 M (200 g) deionized water for 72 h. The calculated molar volume V_m (mm³) of the solution is 75.331×10^3 mm³ at standard density ($\rho_{\text{NaCl}} = 0.00216$ g/mm³) of the NaCl. The chemical potential μ_k (kJ) is calculated considering standard enthalpy change (−411 kJ/mol) of NaCl.

2.4. Experimental observations

2.4.1. Pre-experimental observations

The experiment has been designed to analyse the effect of various roughness values of the film–substrate interface on the interfacial toughness while keeping the film thickness constant for all three samples. The film thickness h for all samples was kept constant with a tolerance of ± 0.004 mm as shown in Table 1. Three samples SI, SII and SIII were prepared with various roughness values (Section 2.1). Roughness at interface can be related to non-dimensional roughness/material parameter (λ) as [41].

$$\lambda = \frac{\Gamma_{IC} W_a}{E_1 R_a^2}$$

where R_a is the amplitude of surface abrasion (roughness) and W_a is the average wavelength of abrasion. $\frac{R_a^2}{W_a}$ is termed as the substrate property while $\frac{\Gamma_{IC}}{E_1}$ is termed as the film property. A case has been designed in which coating thickness is kept constant, while R_a and W_a for three samples (SI, SII and SIII) are varied as shown in Figures 1(a)–(d). For such a case, effect of parameter λ on interface toughness is analysed as given in Table 1. It can be seen that for sample SIII with highest interfacial roughness, λ is lowest, while for sample SI, with lowest interfacial roughness, λ is highest.

Table 1. Pre-experimental data.

Sample no.	h (mm)	R_a (mm)	W_a (mm)	Interfacial roughness R_a^2/W_a (mm)	H (N/mm ²)	σ (GPa)	σ_c (GPa)	E_1 (GPa)	Γ_{7C} (N/mm)	ψ (°)	λ
SI	1.6×10^{-2}	8×10^{-6}	3×10^{-5}	2.1×10^{-6}	3708	3.6	3.4	3.982	0.0249	5.4	2.931
SII	1.9×10^{-2}	5×10^{-5}	3.9×10^{-4}	6.4×10^{-6}	3708	3.6	3.4	3.811	0.0286	5.4	0.825
SIII	1.7×10^{-2}	6.9×10^{-4}	2.2×10^{-3}	2.1×10^{-4}	3708	3.6	3.4	3.939	0.0251	5.4	0.029

2.4.2. Post-experimental observations

Post-experimental results were obtained using a 3D scanning interferometry. The volume of blister has been quantified through surface profiling using interferometry and as per ASTM D-714 specifications as shown in Table 2. The scanning was performed over an area of 3.1×2.32 mm, and these are highlighted by a black circle for all samples as shown in the first column of Table 2. The blisters are spread uniformly over the entire surface of the samples. The surface profiling shows the amplitude and width of blisters. The upward (above reference point) volume of deformed region is calculated for the entire scanned surface which gave the overall extent of blistering. It is found that sample SIII had less blisters compared to the other samples (SI and SII). It has been found that when samples were subjected to

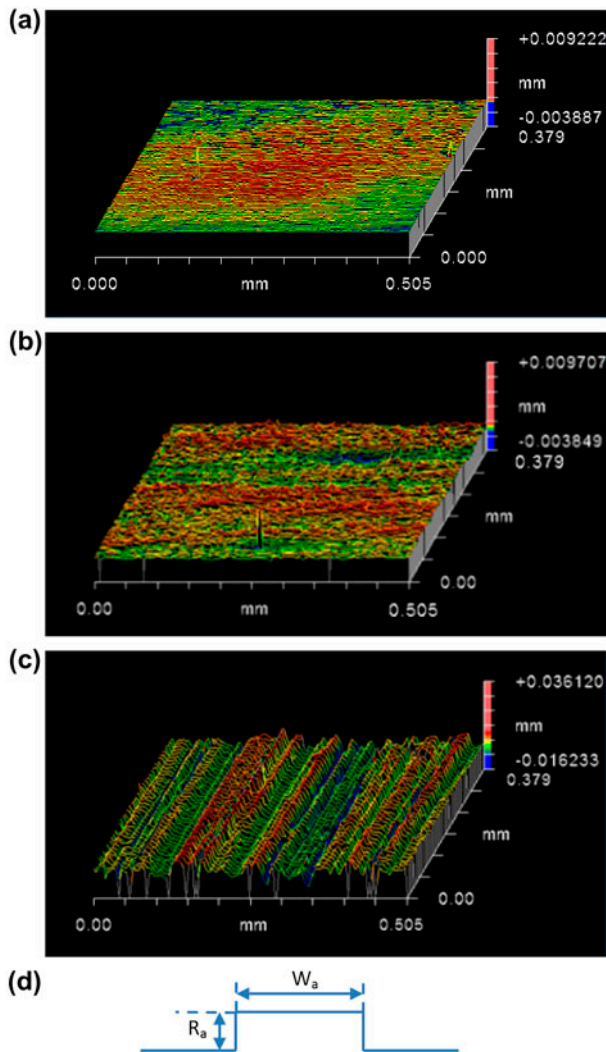


Figure 1. Samples prepared with different interface roughness (a) sample I, (b) sample II, (c) SIII and (d) schematic showing substrate roughness.

Table 2. Sample images, 3D mapping, surface profiling and blistered region volume measurement using interferometer.

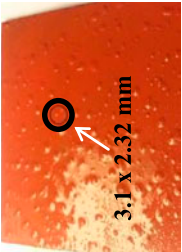
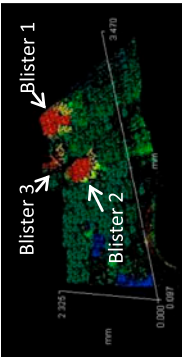
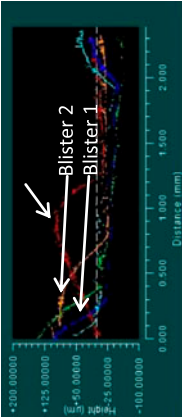

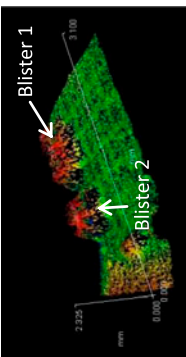
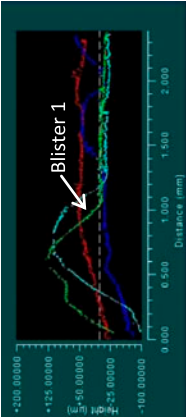

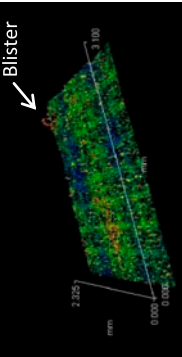
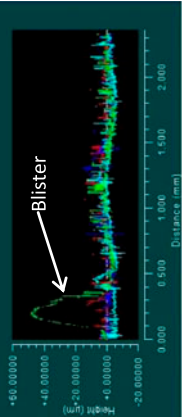
Sample no.	Sample image	3D mapping of circled area on sample image	Surface profiling of circled area	Blistered volume in circled area (mm ³)	ASTM D 714 evaluation
SI: Least rough interface				0.58	Dense
SII				0.38	Medium Dense
SIII: Most rough interface				0.13	Few

Table 3. Post-experimental data.

Sample no.	h (mm)	H (N/mm ²)	Normalized mode adjusted debonding driving force (MADDF), $G/\Gamma_{IC}f(\sigma_c/\sigma)$ (N/mm)
SI	8×10^{-3}	1211	0.0245
SII	1×10^{-2}	1652	0.0248
SIII	1.1×10^{-2}	1817	0.0052

NaCl solution, $\frac{\sigma}{\sigma_c}$ (diffusion-induced stress per unit critical stress) becomes constant with time. Since there is no rise in diffusion-induced stress or mechanical loading (due to constant chemical potential of NaCl solution), ψ becomes constant which then stabilizes the growth of blistered region. Where larger ψ accounts for higher interface toughness $\Gamma(\psi)$, while smaller ψ accounts for lower interface toughness. However, the interface toughness can only be adjusted using proper interface roughness $\frac{R_a^2}{W_a}$ which relates to material/roughness parameter λ . Experimental results showed that sample SIII had highest interfacial toughness due to higher interfacial roughness $\frac{R_a^2}{W_a}$ (lower λ) as compared to samples SI and SII.

Post-experimental values of film micro-hardness and mode-adjusted debond driving force (MADDF) are calculated using equations [42]. These results are provided in Table 3, which also show post-experimental film thickness for all the samples. Comparison of Table 1 (pre-exp.) and Table 3 (post-exp.) shows that sample SIII with lowest λ had lowest MADDF (thus highest interfacial toughness), while sample SI with highest λ had highest MADDF (thus lowest interfacial toughness).

The next section will focus on design of mathematical model for blistering incorporating all the diffusion and fractured mechanics parameters. The mathematical model for blister initiation and propagation is designed based on the experimental observations.

3. Mathematical modelling for blistering

This work is the continuation of research within group as [43–46]. The basic idea of cathodic blistering is similar to that of cathodic delamination. A 3D model representation of cathodic blister initiation and propagation is shown in Figures 2(a) and (b). Delamination and blistering models are often either approached through fracture mechanics or diffusion law concepts. The current research combines both the above concepts to quantify the mechanism of cathodic blistering, as shown in Figures 2(c) and (d). The concept of fracture mechanics for coating debondment is taken from [33].

This research presents growth mechanisms of a single straight-sided blister. The blister growth rate is a function of several parameters i.e. diffusion parameters and mechanics parameters of coating/substrate. If ‘V’ represents the blister growth rate, then

$$V = f \left(\underbrace{c, D_i^*, \mu, \Omega, N_i^*, T, RE_1, v, R_a, W_a, \omega, \sigma, \sigma_c, \Gamma_{IC}, M_B, G, G_m, \delta, F_c, \psi, \alpha, \beta, \Upsilon, \lambda}_{\text{Diffusion parameters}}, \underbrace{\phantom{c, D_i^*, \mu, \Omega, N_i^*, T, RE_1, v, R_a, W_a, \omega, \sigma, \sigma_c, \Gamma_{IC}, M_B, G, G_m, \delta, F_c, \psi, \alpha, \beta, \Upsilon, \lambda}}_{\text{Fracture mechanic parameters}} \right)$$

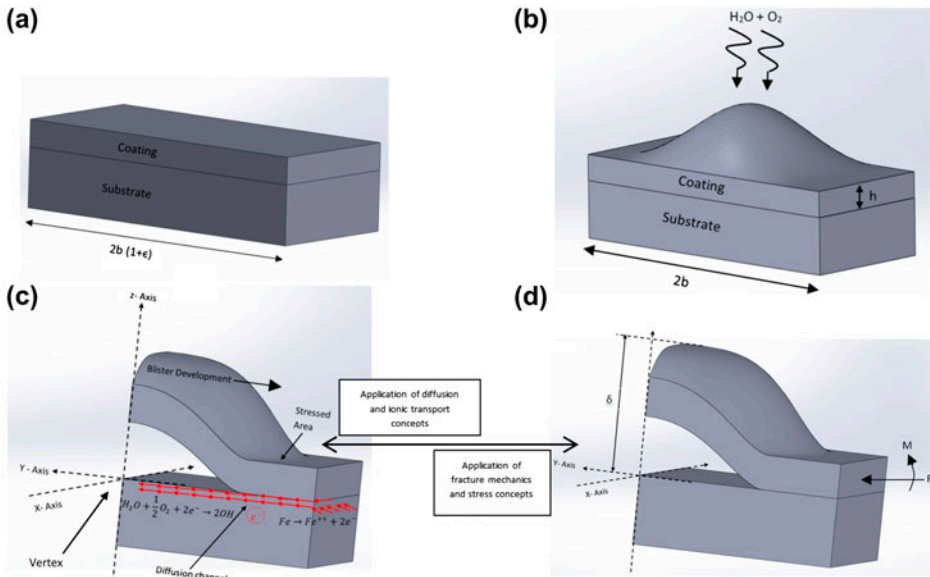


Figure 2. A 3D schematic for a blister on a coated surface using fracture mechanics and diffusion concepts; (a) bonded film, (b) debonded film, (c) cross-sectional view of debonded film showing diffusion mechanism and (d) cross-sectional view of debonded film showing fracture mechanic parameters.

All the above parameters were used during the calculations for developing the governing law for blister propagation.

3.1. Diffusion and ionic transport model

When an infinitely deep steel panel (substrate) coated with a thin film is exposed to a salt solution, the transport of oxygen, water and metal ions takes place, resulting in the formation of an electrochemical cell. Iron is oxidized at the anodic sites, while oxygen is reduced at the cathodic sites, as shown in Figure 2(c). The cathodic-induced areas serve as ‘blister nucleation sites’.[27] The coating starts debonding due to internal stresses as a result of pressurized liquid inside the blister cavity, once a threshold is reached.

This study focuses on the straight sides of the debonded area along $|y| = \pm b$. [35] Consider the debonded area (initial defect) at the metal/coat interface with conditions $|y| \leq b$ and $|x| < \infty$. The flux of species i , in a diluted electrochemical system is given in Equation (1). [9]

$$N_i = -(D_i \nabla c) \quad (1)$$

The term on the right-hand side of Equation (1) represents the diffusion component of the flux formation. Furbeth and Stratmann [10–16] reported that the diffusion coefficients D_i^* of the species at the interface are undergoing cathodic delamination which is two orders smaller in magnitude compared to the aqueous solution. The species inside a blister cavity will exhibit similar behaviour in terms of cathodic delamination magnitude i.e. two orders smaller. Thus, the flux of species inside the blister cavity $N_i^*(y)$ is given as:

$$N_i^*(y) = -(D_i^* \nabla c) \quad (2)$$

The driving force for diffusing species is the chemical potential of that species, so Equation (2) can now be modified using Maxwell-type relation, derivable from expression of Helmholtz free energy as [47]:

$$N_i^*(y) = \frac{D_i^* \nabla c}{RT\Omega} (\nabla \mu(y)) \quad (3)$$

where $\mu(y)$ represents the chemical potential of species along the metal coat interface, Ω represents the partial molar volume of diffusing species. Both of these parameters are related as: $\nabla \mu(y) = -\Omega \nabla \sigma(y)$. The term $\sigma(y)$ is the normal diffusion-induced stress at a location y along the metal/coat interface.[27] This function serves as the basis for the relationship between diffusion and fracture mechanic components of a blistering system.[48] Equation (3) can now be rewritten as:

$$N_i^*(y) = \left(\frac{D_i^* \nabla c}{RT} \right) \cdot \nabla \sigma(y) \quad (4)$$

Equation (4) can be written as:

$$\frac{N_i^*(y)RT}{D_i^* \nabla c} = \nabla \sigma(y) \quad (5)$$

3.2. Fracture mechanics model for blister propagation

For the bonded coating shown in Figure 2(a), the stress (σ) in the film is distributed everywhere and elastic energy (G) stored in the film is zero. As soon as the stress becomes large enough due to excessive liquid pressure and ionic activity inside the blister, the coating film starts to debond, as shown in Figure 2(b). The resultant stress ΔN and a bending moment M_B develops at the coating across its edge at $y = b$. The edges are subjected to tensile loading (stress). At the initiation of cathodic debondment, if σ_c is the critical cathodic debondment stress, then the interfacial stress σ at vertex point, $(x, y, z) = (0, 0, 0)$, must always be equal to or greater than σ_c as

$$\sigma \geq \sigma_c \quad (6)$$

The net stress $\sigma_{\text{net}} = \sigma - \sigma_c$ on the coating can be written as:

$$\sigma_{\text{net}} = \sigma - \sigma_c \quad (7)$$

This developed fracture mechanics approach follows three steps:

- (1) Analysis of normalized stresses including the released elastic energy G and interfacial debondment propagation after blister initiation due to ionic transport. The width of bonded and debonded coating films are assumed to be $2b(1 + \epsilon)$ and $2b$, respectively, as shown in Figure 3(a), where $\epsilon = \frac{1-\nu^2}{E} \sigma$ is the normal plane strain, E is the effective Young's modulus calculated under exposure condition and ν is the Poisson's ratio of the coating film.
- (2) If normalized stresses exceed the critical stress level or if the debonded region is comparatively large enough, then interfacial debondment propagation will take place and the blister will start spreading depending upon the interfacial toughness.

- (3) The toughness functions depend upon the mixed mode parameter (ψ) and can be corrected using two mode adjustment roughness parameters (λ and Υ).

At the frontal area of debonding, $F < F_c$ and $\sigma < \sigma_c$, the coating film remains intact with the substrate (bonded) and local debonding deflection δ is zero. Assuming condition, $h/b \ll 1$ where h is the thickness of coating film and the critical failure at the edge, F_c , is given as [49]:

$$F_c = \frac{\pi^2}{12} \left(\frac{E_1 h}{1 - \nu^2} \right) \left(\frac{h}{b} \right)^2 \tag{8}$$

When the coating film starts to debond from the substrate, the critical stress σ_c is given by [34]:

$$\sigma_c = \frac{F_c}{h} = \left(\frac{\pi}{b} \right)^2 \left(\frac{D}{h} \right) = \frac{\pi^2}{12} \left(\frac{E_1 h}{1 - \nu^2} \right) \left(\frac{h}{b} \right)^2 \tag{9}$$

where D is the flexural rigidity (bending stiffness) of the coating ($D = \frac{E_1 h^3}{12(1 - \nu^2)}$). [35] According to non-linear plate theory, the length of the coat in bonded and debonded forms will be different as part of the length of the coat is utilized in the blister during the process of debonding. The change in length $2b(1 + \epsilon)$ can be written as:

$$\Delta L = 2b(1 + \epsilon) - 2b = 2b\epsilon \tag{10}$$

In order for the coating film to revert to its original position on the substrate, it must satisfy the condition $\Delta L = 2b\epsilon$. Solving Equation (10) yields:

$$\Delta L = \frac{2b(1 - \nu^2)F_c}{E_1 h} + \frac{1}{2} \int_{-b}^b w'^2 dy = \frac{2b(1 - \nu^2)F_c}{E_1 h} + \frac{\pi^2}{8b} \delta^2 \tag{11}$$

Solving Equation (11) for the local deflection, $\delta(y)$ shown in Figure 3(b) (refer Appendix 1)

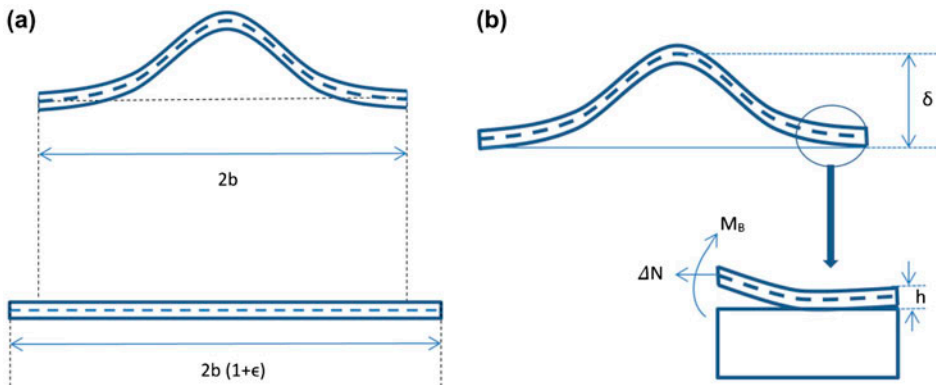


Figure 3. (a) Width of Buckled (top) and unbuckled (bottom) coating film. (b) Geometry and fracture mechanics parameters along interfacial crack of straight edge.[35]

$$\delta(y) = \frac{4b}{\pi} \sqrt{\left(\frac{1-\nu^2}{E_1}\right)} (\sigma - \sigma_c) \quad (12)$$

Under the steady-state condition, at an arbitrary location y , the local deflection, $\delta(y)$ of the coating film can be related by substituting Equation (5) in Equation (12).

$$\delta(y) = \frac{4b}{\pi} \sqrt{\left(\frac{1-\nu^2}{E_1}\right) \left(\frac{N_i^*(y)RT}{D_i^* \nabla c} - \frac{\pi^2}{12} \left(\frac{E_1 h}{1-\nu^2}\right) \left(\frac{h}{b}\right)^2\right)} \quad (13)$$

Simulation results of the stress with respect to distance from the vertex of blister initiation indicate that both stresses and deflections are varied with decaying amplitudes. For $\sigma > \sigma_c$, the bending moment is directly proportional to the second-order derivative of the deflection w , $M_B = Dw''$ at vertex point.[49] Thus,

$$M_B = \frac{1}{2} \sigma_c h^2 \left(\frac{\delta}{h}\right) = \frac{2b}{\pi} \sigma_c h \sqrt{\frac{1-\nu^2}{E_1}} \sigma_{\text{net}} \quad (14)$$

where $\sigma_{\text{net}} = \frac{N_i^* RT}{D_i^* \nabla c} - \frac{\pi^2}{12} \left(\frac{E_1 h}{1-\nu^2}\right) \left(\frac{h}{b}\right)^2$. For the case when, $\sigma \geq \sigma_c$, the released elastic energy, G , is obtained using straightforward algebraic simplifications.[35] G and ΔS relationships for debonding interfaces were first reported in [33–35]. The resultant stress per unit length of the defective edge due to debonding of the coating is given as $\Delta S = \sigma_{\text{net}} h$. G is obtained using Equation (15), considering resultant stress change at the edge of the metal/coating substrate interface

$$G = \frac{(1-\nu^2)h}{2E_1} (\sigma_{\text{net}})(\sigma + 3\sigma_c) = \frac{(1-\nu^2)\Delta S}{2E_1} (\sigma + 3\sigma_c) \quad (15)$$

When the stress σ is very large compared to critical stress σ_c : ($\sigma \gg \sigma_c$) then $G \rightarrow G_m$, where G_m is the elastic energy stored in the bonded film.[35] This situation gives rise to edge delamination and is given in Equation (16):

$$G_m = \frac{(1-\nu^2)h\sigma^2}{2E_1} \quad (16)$$

The ratio G/G_m depends only on σ/σ_c and ν as plotted in Figure 4.

G increases monotonically with σ/σ_c , gradually approaching G_m and flattens out when $\sigma = \sigma_c$, Equation (17)

$$\frac{G}{G_m} = 1 + \frac{\sigma_c}{\sigma} \left(2 - \frac{3\sigma_c}{\sigma}\right) \quad (17)$$

At the start of debonding, when σ/σ_c is only slightly above one, the interface experiences a higher degree of debonding as shown by a sharp rise in G/G_m in Figure 4. Based on characterizing the elastic properties of coating and composite models,[35,42,50] the modified fracture mechanics model developed in this research takes into consideration Dundurs' elastic mismatch parameters (α and β), where α is a function of elastic moduli, β depends on Poisson's ratio and elastic moduli.[51]

Here, $\alpha = \frac{\bar{E}_1 - \bar{E}_2}{\bar{E}_1 + \bar{E}_2}$, where $\bar{E}_i = \begin{cases} \frac{E_i}{1-\nu^2} & (\text{plane strain}) \\ E_i & (\text{plane stress}) \end{cases}$. [49] Note that $\alpha = 0$ when $\bar{E}_1 = \bar{E}_2$. For simplicity, β is set to zero as non-zero β complicates the interfacial

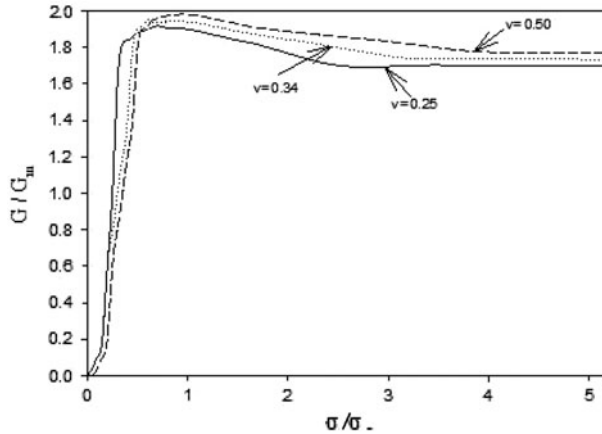


Figure 4. G/G_m as a function of σ/σ_c for various values of ν .

mechanics modelling. Stress intensities along the interface at a distance y from the vertex point of the blister are defined using stress intensity factors: K_1 (mode 1) and K_2 (mode 2). These factors are related to the released energy rate as given in Equation (18):

$$G = \frac{(1 - \nu^2)\Delta N}{2E}(\sigma + 3\sigma_c) = \frac{K_1^2 + K_2^2}{E^*} \tag{18}$$

where $E^{*-1} = [0.5 (\bar{E}_1 + \bar{E}_2)^{-1}]$ for condition $\beta = 0$, $K_1 = \sqrt{E^*G} \cos \psi$, $K_2 = \sqrt{E^*G} \sin \psi$, G and ψ define the plane strain characteristics at the vertex point along the interface. ψ is given in Equation (19) [34]:

$$\psi = \tan^{-1} \left(\frac{K_2}{K_1} \right) = \tan^{-1} \left(\frac{4 + \sqrt{3}\zeta \tan \omega}{-4 \tan \omega + \sqrt{3}\zeta} \right) \tag{19}$$

where ψ is an indicator for the proportion of both the modes K_1 and K_2 as indicated by the ratios in Equation (19). ψ depends upon $\omega(\alpha)$ and the debonding linear deflection parameter δ . The linear deflection per unit coating thickness is given by parameter ζ , where $\zeta = \frac{\delta}{h} = \sqrt{\frac{4}{3} \left(\frac{\sigma}{\sigma_c} - 1 \right)}$. ζ and ω increase with the rise in $\frac{\sigma}{\sigma_c}$ and α , respectively, which eventually results in the increase in ψ . The relationship between ζ and $\frac{\sigma}{\sigma_c}$ and the relationship between ω and α are shown in Figures 5(a) and (b), respectively.

Figure 5(c) shows the curves for mixed mode parameter ψ as a function of σ/σ_c for various values of α , as shown in the following equation. Equation (20) is derived by substituting $\zeta = \frac{\delta}{h} = \sqrt{\frac{4}{3} \left(\frac{\sigma}{\sigma_c} - 1 \right)}$ in Equation (19) (refer Appendix 2)

$$\psi = \tan^{-1} \left[\frac{\left(4 + \sqrt{4 \left(\frac{\sigma}{\sigma_c} - 1 \right) \tan \omega} \right)}{-4 \tan \omega + \sqrt{4 \left(\frac{\sigma}{\sigma_c} - 1 \right)}} \right] \tag{20}$$

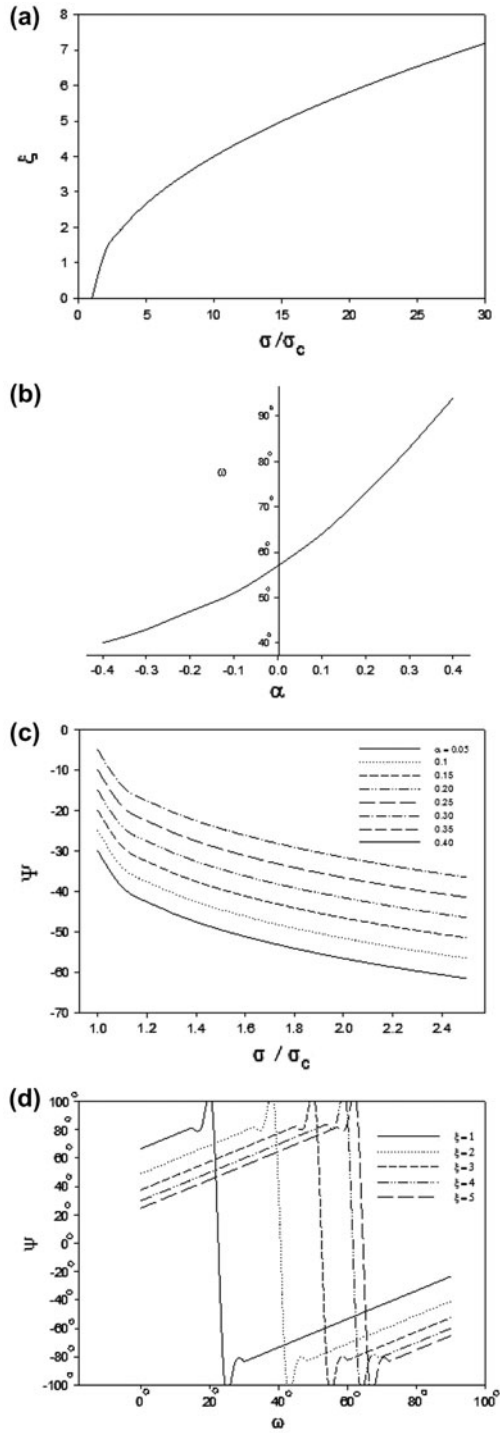


Figure 5. (a) Plot of ξ as a function of σ/σ_c . (b) Plot of ω as a function of α . (c) Curves of mixed mode parameter ψ as a function of σ/σ_c for various values of α . (d) Curves of ψ as a function of ω for various values of ξ .

These curves follow a similar trend to that plotted by Hutchinson et al. [34]. The trend of curves for ψ as a function of ω for various values of ξ is shown in Figure 5(d). The curves show that for the range of values of $\omega(0^\circ \rightarrow 90^\circ)$, ψ varies between $-90^\circ \rightarrow +90^\circ$. The key parameter effecting ψ is ω which depends upon various values of α (the elastic mismatch parameter). At a stage when $\alpha = 0$ ($E_1 = E_2$) and $\omega = 56.3^\circ$, the smooth relative progression of ψ starts. The mixed mode parameter rise is directly related to increases in both ξ and $\frac{\sigma_c}{\sigma}$. When $\psi = -90^\circ$, $K_1 \rightarrow 0$ (mode 1), and the loading effect at the vertex point of the blister becomes purely mode 2. Thus, from Equations (5) to (18), the released energy G increases with the rise in diffusion-induced stress intensity, σ . G is related to the fracture toughness property Γ of the interface as:

$$G = \Gamma(\psi) \quad (21)$$

Larger ψ accounts for higher interfacial toughness that offers increased resistance to blister growth. The mix mode parameter (ψ) depends on σ which indicates that the interfacial toughness Γ increases with the rise in deflection (δ).

3.3. Propagation of blister boundaries using mode adjustment parameters

The diffusion-induced stress σ increases monotonically with an increase in G/G_m for a given blister. However, it is noted that blister growth associated with a rise in σ is non-uniform until the condition $G = \Gamma(\psi)$ is met, where $\Gamma(\psi)$ is the interfacial toughness. The critical stress σ_c decreases with the increase in blister radius b , resulting in the decay of the proportion i.e. the ratio of critical to the induced stresses σ_c/σ . In order to the sake of simplicity in calculations, the reciprocal of σ/σ_c is used in the following sections. Mix mode ψ , and the energy release rate G , at the debonding edge interface, increase with the decrease in σ_c/σ . The debonding edge interfaces are considered to be tougher in mode 2 rather than in mode 1. Equation (22) is derived by further simplifying Equation (20). The curves obtained using Equation (22) show the relationship of σ_c/σ as a function of ψ for various values of ω , as shown in Figure 6(a) (refer Appendix 3)

$$\frac{\sigma_c}{\sigma} = \frac{1}{\sqrt{\frac{2}{\tan(\psi-\omega)} + 1}} \quad (22)$$

Based on Hutchinson's concept of the toughness function for modelling, the ratio of mode 2 to mode 1 toughness,[35] a specific toughness function and the concept of mode-adjusted debondment driving force (MADDF) is introduced. $\Gamma(\psi)$ increases from mode 1 ($\psi = 0^\circ$) to mode 2 ($\psi = \pm 90^\circ$) with the increase in ψ , ($0^\circ - |\pm 90^\circ|$) which in turn depends on σ_c/σ . If the interfacial toughness variable to analyse the blister propagation is considered, then the following representation may be utilized:[34]

$$\Gamma(\psi) = \Gamma_{1C}(\psi)f(\psi) \quad (23)$$

where Γ_{1C} is the interfacial toughness for mode 1 and $f(\psi) \rightarrow f\left(\frac{\sigma_c}{\sigma}\right)$. [34] The toughness function is given by:

$$f\left(\frac{\sigma_c}{\sigma}\right) = -3\left(\frac{\sigma_c}{\sigma}\right)^2 + 2\left(\frac{\sigma_c}{\sigma}\right) + 1 \quad (24)$$

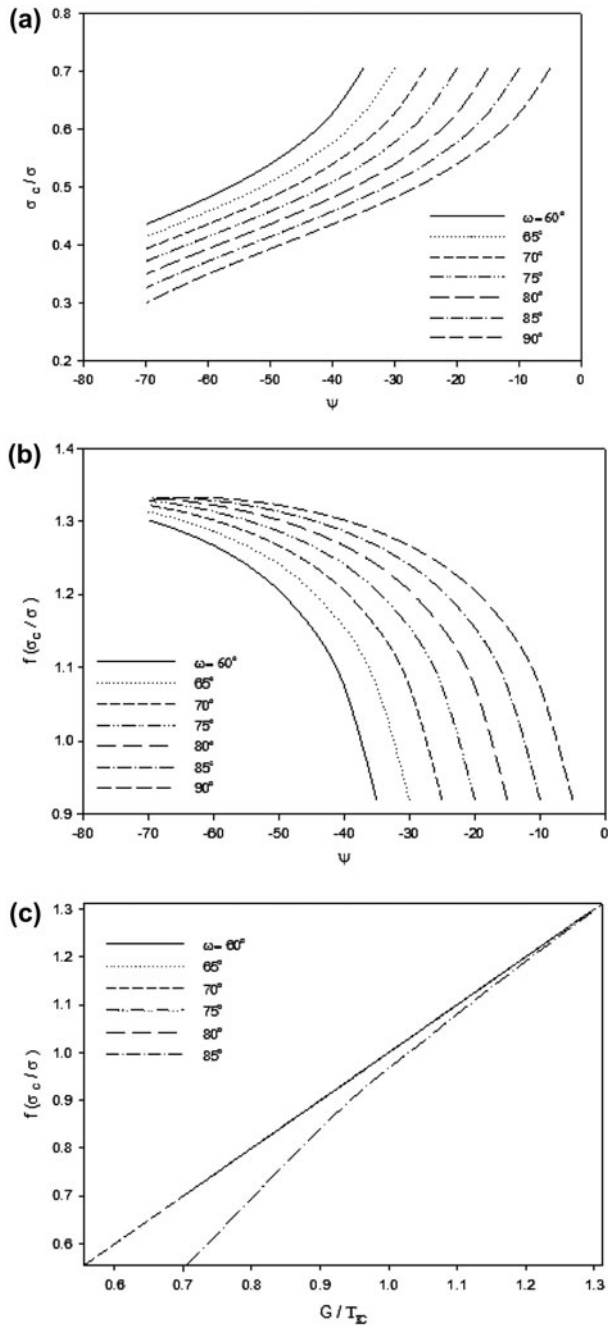


Figure 6. (a) Curves of σ_c/σ as a function of ψ for various values of ω . (b) Curves of $f(\frac{\sigma_c}{\sigma})$ as a function of ψ for various values of ω . (c) Curves of $f(\frac{\sigma_c}{\sigma})$ as a function of G/Γ_{IC} for various values of ω .

The second-order quadratic Equation (24) is derived from Equation (17). Plots of $f(\frac{\sigma_c}{\sigma})$ as a function of ψ are taken for various values of ω as shown in Figure 6(b). This shows a decreasing trend of $f(\frac{\sigma_c}{\sigma})$ for various values of ψ as ω increases from $60^\circ \rightarrow 90^\circ$ and ψ from $-90^\circ \rightarrow 0^\circ$. A higher value of $f(\frac{\sigma_c}{\sigma})$ accounts for the increased value of proportion ($\frac{G}{\Gamma_{IC}}$) as in the following relationship, which has been given in Figure 6(c):

$$\frac{G}{\Gamma_{IC}} = f\left(\frac{\sigma_c}{\sigma}\right)$$

When $f(\frac{\sigma_c}{\sigma}) = 1$, then $\Gamma(\psi) = \Gamma_{IC}$, which corresponds to the criterion $K_I = K_{IC}$, and coincides with the classical theory of no-mode dependence.[34] The trend of plots in Figure 6(c) demonstrates a linear progression is achieved when $f(\frac{\sigma_c}{\sigma}) = 1$ at $G \rightarrow \Gamma_{IC}$.

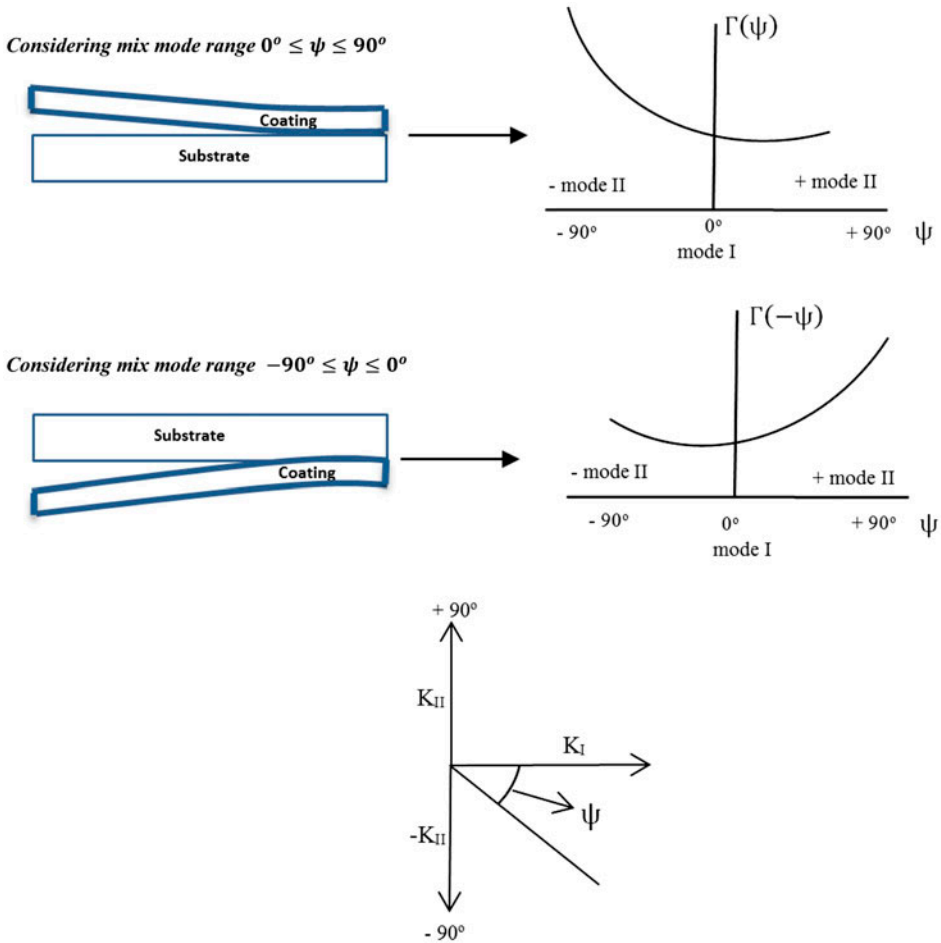


Figure 7. Schematic of coating/substrate interface toughness as a function of mode mix. When coating lies above the substrate the interface toughness is $\Gamma(\psi)$. When the coating lies below the substrate the interface toughness is $\Gamma(-\psi)$.

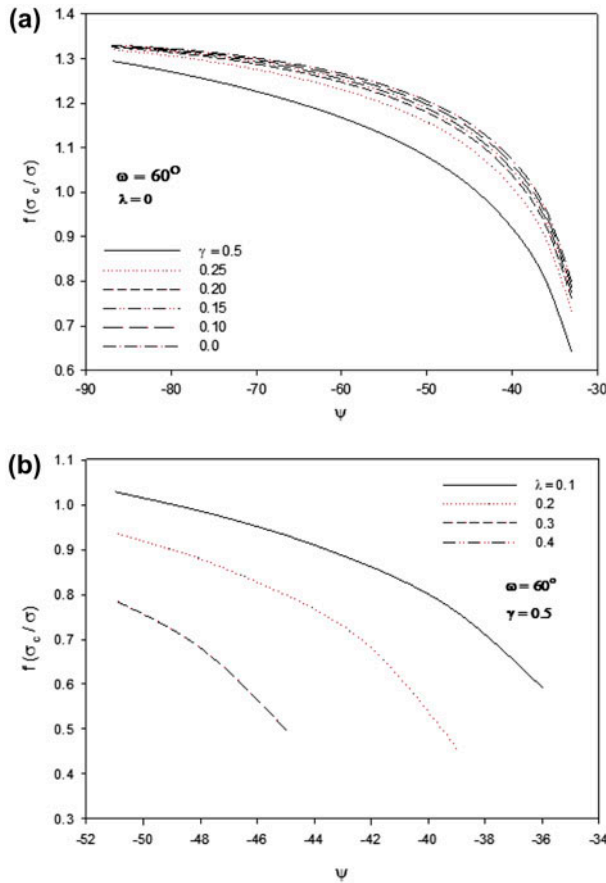


Figure 8. (a) Curves of $f(\frac{\sigma_c}{\sigma})$ as a function of $|\psi|$ for various values of ω for condition $\lambda = 0$ and $\omega = 60^\circ$. (b) Curves of $f(\frac{\sigma_c}{\sigma})$ as a function of $|\psi|$ for various values of ω for condition $\Upsilon = 0.5$ and $\omega = 60^\circ$.

This function incorporates the rise in the value of relative proportion of mode 2 to mode 1.

For a much wider and deeper analysis of blister propagation, the ratio of mode 2 to mode 1 is considered to be a function of two phenomenological parameters, λ and Υ . Equation (24) can be modified in the form of a two-parameter family of toughness functions as given below (refer Appendix 4)

$$f\left(\frac{\sigma_c}{\sigma}\right) = -3 \left(\frac{1}{\sqrt{\frac{2(1-\Upsilon)}{\tan(\psi(1-\lambda)-\omega)} + 1}} \right)^2 + 2 \left(\frac{1}{\sqrt{\frac{2(1-\Upsilon)}{\tan(\psi(1-\lambda)-\omega)} + 1}} \right) + 1 \quad (25)$$

where Υ and λ can be related to fracture interface roughness as in [52,53].

In order to fully understand the propagation of blister boundaries, the simulation results for two mix mode ranges ($-90^\circ \leq \psi \leq 0^\circ$ and $0^\circ \leq \psi \leq 90^\circ$) have been separately analysed as shown in Figure 7.

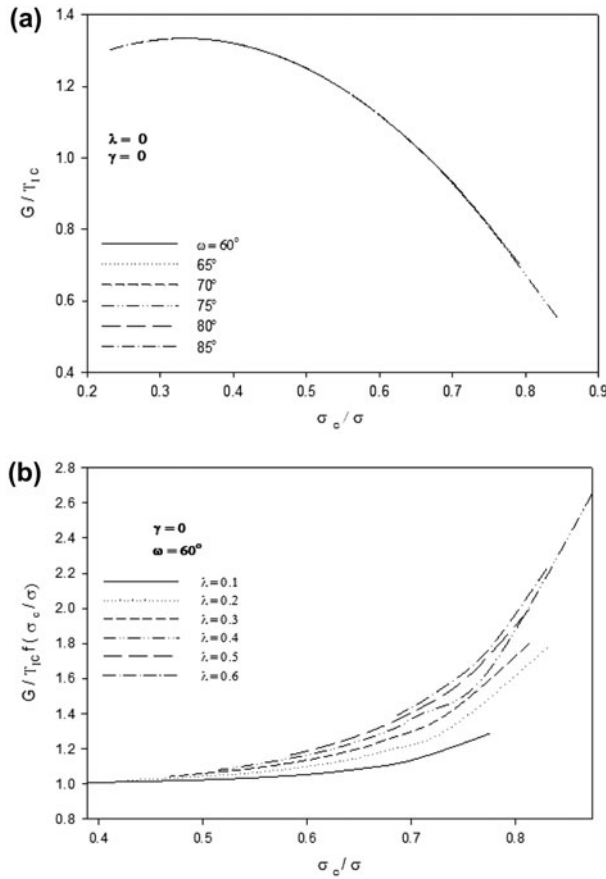


Figure 9. Graphs for condition $-90^\circ \leq \psi \leq 0^\circ$. (a) Curves of G/Γ_{IC} as a function of σ_c/σ for condition $\lambda = \Upsilon = 0$. (b) Curves of $G/\Gamma_{IC}f(\sigma_c/\sigma)$ as function of σ_c/σ for condition $\Upsilon = 0$ and $\omega = 60^\circ$. (c) Curves of $G/\Gamma_{IC}f(\sigma_c/\sigma)$ as function of σ_c/σ for condition $\lambda = 0$ and $\omega = 60^\circ$. (d) Curves of $G/\Gamma_{IC}f(\sigma_c/\sigma)$ as function of σ_c/σ for various values of Υ and λ and $\omega = 60^\circ$.

Considering mix mode range $-90^\circ \leq \psi \leq 0^\circ$, if $0 \leq \Upsilon < 1$ and $0 \leq \lambda < 1$, then Equation (25) follows the criterion $f(\frac{\sigma_c}{\sigma}) > 0$. When $\Upsilon = 1$, Equation (25) exhibits quadratic behaviour. When $f(\frac{\sigma_c}{\sigma}) = 0$, the system of equations becomes unstable; therefore, Υ should always be less than 1.

Similarly, when $\lambda = 1$ and $\psi < \omega$, the system becomes unstable as $f(\frac{\sigma_c}{\sigma}) = \text{infinity}$; hence, both conditions should be avoided. The angular deflection of ψ is plotted in Figures 8(a) and (b) for a constant value of Υ at 0.5 where $f(\frac{\sigma_c}{\sigma})$ is a function of both parameters λ (variable) and Υ (constant).

The relation $G/\Gamma_{IC} = f(\psi)$ is termed as mode adjustment debondment progression equation in terms of Γ_{IC} . For the case Υ and $\lambda = 0$, the curves for G/Γ_{IC} as a function of σ_c/σ are shown in Figure 9(a) for various values of ω . The trend of the graph shows a decaying progression until $\psi + \omega > 90^\circ$. This decaying behaviour is due to the term

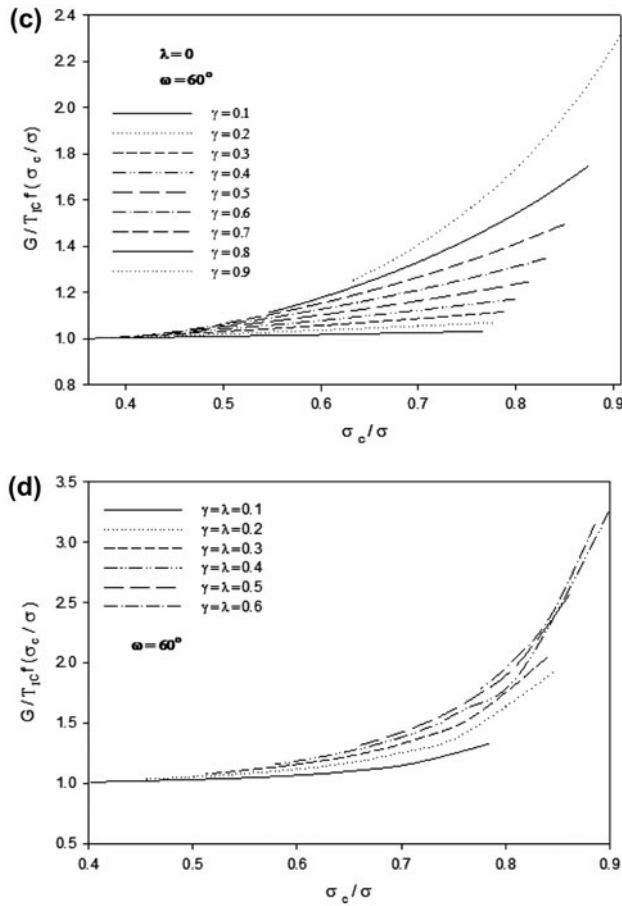


Figure 9. (Continued).

$\sqrt{2/\tan(\psi - \omega)}$ in Equation (22), which shows an increasing behaviour for values of ψ from $-90^\circ \rightarrow 0^\circ$. An overall decay for σ_c/σ is shown at the values of G/Γ_{IC} . Curves for normalized MADDF, $G/\Gamma_{IC}f(\sigma_c/\sigma)$ at various values of Υ and λ are shown in Figures 9(b)–(d). The increase in σ_c/σ , Figures 9(b)–(d), is linked to the increase in the curves for normalized debondment driving force. The interfacial toughness $G = \Gamma_{IC}f(\psi)$ is higher towards the bottom of the curves (close to 1 along the vertical axis). The peak values of the curves correspond to mode 1 ($\psi = 0^\circ$) of the interfacial toughness, while the lowest values correspond to mode 2 ($\psi = -90^\circ$). Depending upon Υ and λ , the mix mode proportion is decided between mode 1 and mode 2. Higher values of Υ and λ take into account the corresponding rise in $G/\Gamma_{IC}f(\sigma_c/\sigma)$, resulting in lower interfacial toughness, G , which is close to mode 1. Lower values of Υ and λ , for instance 0.1, will generate higher interfacial toughness. When $f(\frac{\sigma_c}{\sigma}) < 1$, the normalized debondment driving force, $G/\Gamma_{IC}f(\sigma_c/\sigma)$ becomes high resulting in unstable growth of blister. This condition continuous till $f(\sigma_c/\sigma) = 1$ is met as shown in Table 4. This behaviour is linked to the rise in relative proportion of mode 2 to mode 1, and also to ψ and G according to Equation (23). The simulation values for this behaviour are shown in Table 4.

Table 4. Simulation values for $-90^\circ \leq \psi \leq 0^\circ$.

Initial conditions: $\omega = 60^\circ, \Upsilon = \lambda = 0.2$			
ψ ($^\circ$)	G/Γ_{IC}	$f(\sigma_c/\sigma)$	$G/\Gamma_{IC}f(\sigma_c/\sigma)$
-39	1.0514	0.5471	1.9217
-42	1.1114	0.7894	1.4079
-45	1.1547	0.9096	1.2695
-48	1.1877	0.9874	1.2029
-51	1.2137	1.0435	1.1631
-54	1.2349	1.0866	1.1365
-57	1.2523	1.1210	1.1172
-60	1.2670	1.1492	1.1025
-63	1.2794	1.1730	1.0908
-66	1.2901	1.1933	1.0811
-69	1.2992	1.2108	1.0730
-72	1.3070	1.2262	1.0659
-75	1.3137	1.2398	1.0596
-78	1.3194	1.2519	1.0539
-81	1.3241	1.2627	1.0486
-84	1.3279	1.2725	1.0435
-87	1.3307	1.2813	1.0385
-90	1.3325	1.2893	1.0335

Table 5. Simulation values for $0^\circ \leq \psi \leq 90^\circ$.

ψ ($^\circ$)	Initial conditions: $\omega = 60^\circ, \Upsilon = \lambda = 0.2$			Initial conditions: $\omega = 65^\circ, \Upsilon = \lambda = 0.2$		
	G/Γ_{IC}	$f(\sigma_c/\sigma)$	$G/\Gamma_{IC}f(\sigma_c/\sigma)$	G/Γ_{IC}	$f(\sigma_c/\sigma)$	$G/\Gamma_{IC}f(\sigma_c/\sigma)$
63	1.220	–	–	–	–	–
66	1.268	–	–	1.148	–	–
69	1.294	–	–	1.240	–	–
72	1.310	–	–	1.278	–	–
75	1.320	–	–	1.300	–	–
78	1.326	1.220	1.087	1.314	–	–
81	1.330	1.268	1.049	1.323	–	–
84	1.332	1.294	1.029	1.328	1.214	1.094
87	1.333	1.310	1.017	1.331	1.265	1.052
90	1.332	1.320	1.009	1.333	1.292	1.031

Considering mix mode range $0^\circ \leq \psi \leq 90^\circ$, if σ_c/σ is a function of ψ , then G/Γ_{IC} shows an increasing trend for various values of $\lambda = 0.1, 0.2, 0.3$ and $\Upsilon = 0$ as shown in Figure 10(a). Curves of the normalized debondment driving force, $G/\Gamma_{IC}f(\sigma_c/\sigma)$ for various values of Υ and λ are shown in Figures 10(b)–(d). The curves in Figure 10(b) show a drop in the trend of $G/\Gamma_{IC}f(\sigma_c/\sigma)$ for decreasing values of λ when $\Upsilon = 0$ and $\omega = 60^\circ$. The curves do not fit for $\lambda > 0.3$, as the term $\sqrt{\frac{2(1-\Upsilon)}{\tan(\psi(1-\lambda)-\omega)}}$ in Equation (25) shows unstable results. When $\lambda = 0$ and $\omega = 60^\circ$, then curves show an increasing trend in debondment driving force, $G/\Gamma_{IC}f(\sigma_c/\sigma)$ as a function of $f(\frac{\sigma_c}{\sigma})$ for various values of Υ . It is noted that for $0^\circ \leq \psi \leq 90^\circ$, the main mode adjustment parameter is only λ and a higher λ value compared to Υ increases the debondment

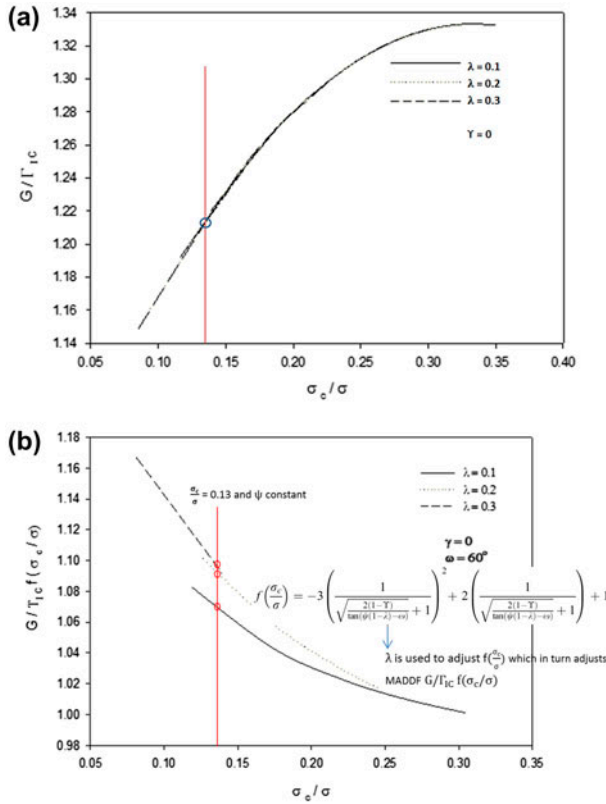


Figure 10. Graphs for condition: $0^\circ \leq \psi \leq 90^\circ$. (a) Curves of G/Γ_{IC} as a function of σ_c/σ for condition: $\lambda = \Upsilon = 0$. (b) Curves of $G/\Gamma_{IC}f(\sigma_c/\sigma)$ as function of σ_c/σ for condition: $\Upsilon = 0$ and $\omega = 60^\circ$. (c) Curves of $G/\Gamma_{IC}f(\sigma_c/\sigma)$ as function of σ_c/σ for condition: $\lambda = 0$ and $\omega = 60^\circ$. (d) Curves of $G/\Gamma_{IC}f(\sigma_c/\sigma)$ as function of σ_c/σ for various values of Υ and λ and $\omega = 60^\circ$.

driving force. The system gives unstable results after $\lambda = \Upsilon = 0.3$, as shown in Figure 10(d). Consequently, an increase in interfacial toughness G is observed from mode 1 to mode 2 (close to 1 along vertical axis). The simulation results for this behaviour are shown in Table 5 for $\lambda = \Upsilon = 0.2$, $\omega = 60^\circ$ and 65° , which shows unstable results for $\psi < 78^\circ$ and 84° , respectively. The sign ‘-’ in Table 5 corresponds to unstable values. The higher $\alpha (> 0)$ accounts for larger ω which, in turn, directly relates to the interfacial toughness, G . It is clear from Figure 5(d) that ω increases with higher value of ζ which, in turn, inversely relates to $f(\sigma_c/\sigma)$. An increase in ω encounters an increase in ζ but reduces $f(\sigma_c/\sigma)$ functionality. This phenomenon is shown in Table 5 for $\omega = 60^\circ$ and 65° .

From above two mix mode ranges $-90^\circ \leq \psi \leq 0^\circ$ and $0^\circ \leq \psi \leq 90^\circ$, it is evident that the governing non-dimensional roughness parameter λ plays a key role in evaluating MADDF, $G/\Gamma_{IC}f(\sigma_c/\sigma)$ (thus interfacial toughness) given a fixed value of Υ .

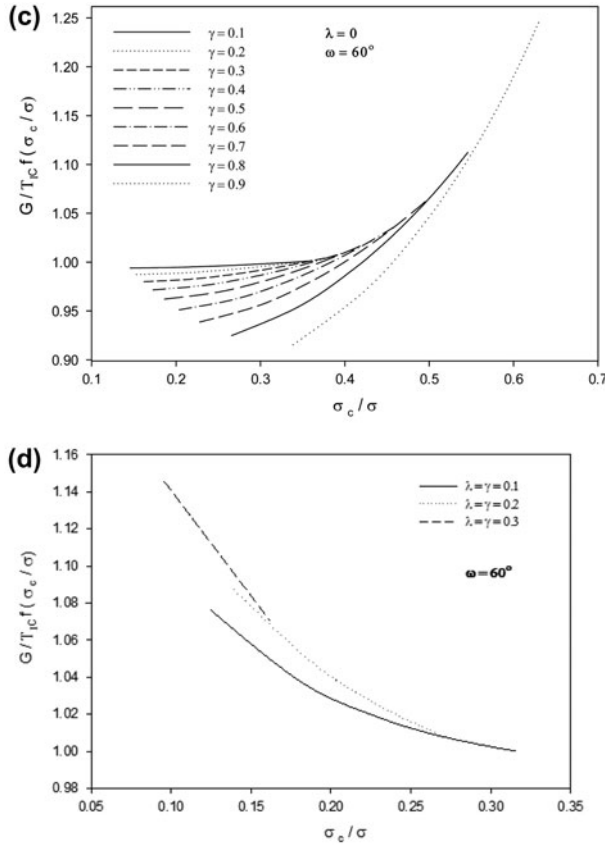


Figure 10. (Continued).

4. Validation of mathematical model using experimental results

The experiment (Section 2) follows the mix mode range criterion $0^\circ \leq \psi \leq 90^\circ$ in which coating lies above the substrate. Thus, all the simulation results under the above criterion will be considered for the validation of mathematical model for blistering.

- (i) For mix mode range $0^\circ \leq \psi \leq 90^\circ$, Figure 10(b) shows that MADDF $G/\Gamma_{ICf}(\sigma_c/\sigma)$ is lower for lower values of λ . For $\lambda = 0.1$, MADDF is lowest (highest interfacial toughness), while for $\lambda = 0.3$, MADDF is highest (lowest interfacial toughness). Experimental results showed similar behaviour in which comparison of Table 1 (pre-exp.) and Table 3 (post-exp.) showed that sample SIII with lowest λ had lowest MADDF (thus highest interfacial toughness), while sample SI with highest λ had highest MADDF (thus lowest interfacial toughness).
- (ii) In Figure 10(b), for constant $\sigma_c/\sigma = 0.13$, ψ is constant (as ψ depends on σ_c/σ); however, ψ can be adjusted using λ as per Equation (25). Similar behaviour was also observed for experiment data in Table 1. Table 1 shows mix mode parameter $\psi = 5.4^\circ$ (which lies in the mix mode range

$0^\circ \leq \psi \leq 90^\circ$) which is constant for all samples (SI, SII and SIII). This constant behaviour of ψ is due to constant diffusion-induced stress ($\sigma = 3.6$ GPa) and critical stress ($\sigma_c = 3.4$ GPa). The stresses remain constant because chemical potential is constant for 11.1 M NaCl solution.

- (iii) In Figure 10(a), the trends for G/Γ_{IC} show no change in behaviour for various values of λ (0.3, 0.2 and 0.1). Experimental results in Table 1 show the similar behaviour where Γ_{IC} remains constant for all samples having different values of λ (2.93, 0.82 and 0.029). The reason behind this behaviour is that Γ_{IC} is a coating property which varies with variation in thickness of film (which is constant in experiment) and has negligible effects with the variation in interface roughness.

5. Conclusions

A comprehensive unified model has been developed to explore the debonding failure mechanisms of blistering. Initial calculations developed the mechanisms for ionic transport of species in to the blister cavity resulting in debonding of the coating from substrates.

Further calculations were performed to explain the mechanics of straight-sided blistering subject to equi-biaxial tensile stresses. The principal equations for both the components were combined to form a governing law for blister propagation based on specific toughness functions and mode adjustment parameters. The following, with regard to cathodic blistering, has been concluded based on the results obtained through the model developed during this research.

- The normalized stresses, σ along the substrate coat interface is a function of chemical potential of the diffusing species.
- If normalized stresses exceed the critical stress level σ_c or if the debonded region is comparatively large enough, then interfacial debondment propagation will take place and blistering will initiate and then spread if and when the interfacial toughness reduces.
- The interfacial toughness depends on the elastic mismatch parameters α and the related angular deflection ω . The curves show that, for the range of values of $\omega(0^\circ \rightarrow 90^\circ)$, the mix mode parameter ψ will vary between $-90^\circ \rightarrow +90^\circ$.
- The specific toughness functions and the concept of mode-adjusted interfacial debondment growth define the propagation of blister boundaries. The interfacial toughness, G increases from mode 1 ($\psi = 0^\circ$) to mode 2 ($\psi = \pm 90^\circ$) with the increase in ψ , $(0^\circ - |\pm 90^\circ|)$ which in turn depends on σ_c/σ .
- The mode 2 to mode 1 proportion is considered to be a function of two mode adjustment parameters, λ and Υ . Curves of normalized MADDF, $G/\Gamma_{IC}f(\sigma_c/\sigma)$ for various values of Υ and λ depend upon the function $f(\sigma_c/\sigma)$. The two parameter toughness functions are useful for analysing the toughness of debonded edge interfaces, which are considered to be tougher in mode 2 ($\psi = \pm 90^\circ$) compared to mode 1 ($\psi = 0^\circ$).

Acknowledgement

This research is joint funded by the Defence Science & Technology Laboratory (DSTL) and Bournemouth University UK, the authors acknowledge their support and contributions.

References

- [1] Matthews A, Leyland A. Hybrid techniques in surface engineering. *Surf. Coat. Technol.* 1995;71:88–92.
- [2] Edavan RP, Kopinski R. Corrosion resistance of painted zinc alloy coated steels. *Corros. Sci.* 2009;51:2429–2442.
- [3] Subanovic M, Naumenko D, Kamruddin M, Meier G, Singheiser L, Quadackers WJ. Blistering of MCrAlY-coatings in H₂/H₂O-atmospheres. *Corros. Sci.* 2009;51:446–450.
- [4] Raja VS, Gayathiri Devi R, Venugopal A, Debnath NC, Giridhar J. Evaluation of blistering performance of pigmented and unpigmented alkyd coatings using electrochemical impedance spectroscopy. *Surf. Coat. Technol.* 1998;107(1):1–11.
- [5] Al-Fadhli HY, Stokes J, Hashmi MSJ, Yilbas BS. HVOF coating of welded surfaces: Fatigue and corrosion behaviour of stainless steel coated with Inconel-625 alloy. *Surf. Coat. Technol.* 2006;200:4904–4908.
- [6] Prawoto Y. Unified model for blister growth in coating degradation using weight function and diffusion concepts. *Mater. Corros.* 2012;64:794–800.
- [7] Allahar KN. Mathematical modeling of disbanded coating and cathodic delamination systems. Gainesville (FL): University of Florida; 2003.
- [8] Allahar KN, Orazem ME. On the extension of CP models to address cathodic protection under a delaminated coating. *Corros. Sci.* 2009;51:962–970.
- [9] Allahar KN, Orazem ME, Ogle K. Mathematical model for cathodic delamination using a porosity–pH relationship. *Corros. Sci.* 2007;49:3638–3658.
- [10] Fürbeth W, Stratmann M. The delamination of polymeric coatings from electrogalvanised steel – a mechanistic approach. *Corros. Sci.* 2001;43:207–227.
- [11] Fürbeth W, Stratmann M. The delamination of polymeric coatings from electrogalvanised steel – a mechanistic approach. *Corros. Sci.* 2001;43:229–241.
- [12] Fürbeth W, Stratmann M. Investigation of the delamination of polymer films from galvanized steel with the Scanning Kelvinprobe. *Fresen. J. Anal. Chem.* 1995;353:337–341.
- [13] Fürbeth W, Stratmann M. Scanning Kelvinprobe investigations on the delamination of polymeric coatings from metallic surfaces. *Prog. Org. Coat.* 2000;39:23–29.
- [14] Fürbeth W, Stratmann M. The delamination of polymeric coatings from electrogalvanised steel – a mechanistic approach. *Corros. Sci.* 2001;43:207–227.
- [15] Fürbeth W, Stratmann M. The delamination of polymeric coatings from electrogalvanised steel – a mechanistic approach. *Corros. Sci.* 2001;43:229–241.
- [16] Fürbeth W, Stratmann M. The delamination of polymeric coatings from electrogalvanised steel – a mechanistic approach. *Corros. Sci.* 2001;43:243–254.
- [17] Grundmeier G, Schmidt W, Stratmann M. Corrosion protection by organic coatings: electrochemical mechanism and novel methods of investigation. *Electrochim. Acta.* 2000;45:2515–2533.
- [18] Hausbrand R, Stratmann M, Rohwerder M. The physical meaning of electrode potentials at metal surfaces and polymer/metal interfaces: consequences for delamination. *J. Electrochem. Soc.* 2008;155:C369–C379.
- [19] Hausbrand R, Stratmann M, Rohwerder M. Corrosion of zinc–magnesium coatings: mechanism of paint delamination. *Corros. Sci.* 2009;51:2107–2114.
- [20] Huang M-W, Allely C, Ogle K, Orazem ME. A mathematical model for cathodic delamination of coated metal including a kinetic pH–porosity relationship. *J. Electrochem. Soc.* 2008;155(5):C279–C292.
- [21] Leidheiser H. Cathodic delamination of polybutadiene from steel – a review. *J. Adhes. Sci. Technol.* 1987;1:79–98.
- [22] Leidheiser H Jr. The mechanism for the cathodic delamination of organic coatings from a metal surface. *Prog. Org. Coat.* 1983;11:19–40.

- [23] Leng A, Streckel H, Hofmann K, Stratmann M. The delamination of polymeric coatings from steel. Part 3: effect of the oxygen partial pressure on the delamination reaction and current distribution at the metal/polymer interface. *Corros. Sci.* 1998;41:599–620.
- [24] Leng A, Streckel H, Stratmann M. The delamination of polymeric coatings from steel. Part 1: calibration of the Kelvinprobe and basic delamination mechanism. *Corros. Sci.* 1998;41:547–578.
- [25] Ogle K, Morel S, Meddahi N. An electrochemical study of the delamination of polymer coatings on galvanized steel. *Corros. Sci.* 2005;47:2034–2052.
- [26] Rohwerder M, Hornung E, Stratmann M. Microscopic aspects of electrochemical delamination: an SKPFM study. *Electrochim. Acta.* 2003;48:1235–1243.
- [27] Chuang TJ, Nguyen T, Lee S. Micro-mechanic model for cathodic blister growth in painted steel. *J. Coat. Technol.* 1999;71:75–85.
- [28] Pommersheim JM, Nguyen T, Hartzfeld K. Prediction of blistering in coating systems. In: Bierwagen GP, editor. ACS Symposium Series. Eishngotn: ACS Publications; 1998. p. 137–150.
- [29] Martin JW. Methodologies for predicting the service lives of coating systems. Vol. 172. Philadelphia (PA): DIANE Publishing; 1994.
- [30] Leidheiser H Jr. Whitney award lecture-1983: towards a better understanding of corrosion beneath organic coatings. *Corrosion.* 1983;39:189–201.
- [31] Nguyen T, Hubbard J, Pommersheim J. Unified model for the degradation of organic coatings on steel in a neutral electrolyte. *J. Coat. Technol.* 1996;68:45–56.
- [32] Chuang T-J, Nguyen T, Lee S. Micro-mechanic model for cathodic blister growth in painted steel. *J. Coat. Technol.* 1999;71:75–85.
- [33] Hutchinson J, Suo Z. Mixed mode cracking in layered materials. *Adv. Appl. Mech.* 1992;29:63–191.
- [34] Hutchinson J, Thouless M, Liniger E. Growth and configurational stability of circular, buckling-driven film delaminations. *Acta Metall. Mater.* 1992;40:295–308.
- [35] Hutchinson JW. Stresses and failure modes in thin films and multilayers. Lecture notes. Copenhagen: Notes for a Dcamm Course. Technical University of Denmark, Lyngby; 1996. Available from: <http://www.seas.harvard.edu/hutchinson/papers/462-5.pdf>
- [36] Prawoto Y, Kamsah N, Mat Yajid MA, Ahmad Z. Energy density mechanics applied to coating blistering problems. *Theor. Appl. Fract. Mech.* 2011;56:89–94.
- [37] Prawoto Y, Dillon B. Failure analysis and life assessment of coating: the use of mixed mode stress intensity factors in coating and other surface engineering life assessment. *J. Fail. Anal. Prevent.* 2012;12:190–197.
- [38] Prawoto Y, Onn IH. Modified Fourier solution for diffusion governing law applied to blister formation and development. *Comput. Mater. Sci.* 2012;62:105–109.
- [39] Prawoto Y, Onn IH. Application of J -integral concept on blister coating problem. *Eng. Fract. Mech.* 2012;92:114–125.
- [40] Sarikaya O. Effect of some parameters on microstructure and hardness of alumina coatings prepared by the air plasma spraying process. *Surf. Coat. Technol.* 2005;190:388–393.
- [41] Hutchinson JW. Mixed mode fracture mechanics of interfaces. *Met. Ceram. Interfaces.* 1990;295–306.
- [42] Volinsky A, Moody N, Gerberich W. Interfacial toughness measurements for thin films on substrates. *Acta Mater.* 2002;50:441–466.
- [43] Saeed A, Khan Z, Smith R, Clark M, Nel M. Non-destructive material characterisation and material loss evaluation in large historic military vehicles. *Insight Non Destr. Test. Cond. Monit.* 2011;53:382–386.
- [44] Saeed A, Khan ZA. Corrosion mapping of historic military vehicles using the TD Focus-Scan. *ndtnews*; 2010.
- [45] Saeed A, Khan Z, Hadfield M, Davies S. Material characterisation and real time wear evaluation of pistons and cylinder-liners of the Tiger 131 Military Tank. *Tribol. Trans.* 2013;56:637–644.
- [46] Saeed A, Khan ZA, Montgomery E. Corrosion damage analysis and material characterization of sherman and centaur – the historic military tanks. *Mater. Perform. Character.* 2013;2(1):1–16.
- [47] Xuan F-Z, Shao S-S, Wang Z, Tu S-T. Influence of residual stress on diffusion-induced bending in bilayered microcantilever sensors. *Thin Solid Films.* 2010;518:4345–4350.

- [48] Weber N, Goldstein M. Stress-induced migration and partial molar volume of sodium ions in glass. *J. Chem. Phys.* 1964;41:2898.
- [49] Hutchinson JW. *Mechanics of thin films and multilayers.* Solid Mechanics. Copenhagen: Technical University of Denmark; 1996.
- [50] Jensen HM. The blister test for interface toughness measurement. *Eng. Fract. Mech.* 1991;40:475–486.
- [51] Schmauder S, Meyer M. Correlation between Dundurs' parameters and elastic constants. *Z. Metallkd.* 1992;83:525.
- [52] Nazir MH, Khan ZA, Stokes K. Optimisation of interface roughness and coating thickness to maximise coating-substrate adhesion – A failure prediction and reliability assessment modelling. *J. Adhes. Sci. Technol.* Forthcoming. doi: [10.1080/01694243.2015.1026870](https://doi.org/10.1080/01694243.2015.1026870)
- [53] Nazir MH, Khan ZA, Stokes K. Modelling of metal-coating delamination incorporating variable environmental parameters. *J. Adhes. Sci. Technol.* 2014;1–32. Ahead-of-print.

Appendix 1. Derivation of Equation (12)

$$\Delta L - \frac{2b(1 - \nu^2)F_c}{E_1 h} = \frac{\pi^2}{8b} \delta^2$$

$$\delta^2 = \frac{16b^2(2b\epsilon)}{\pi} - \frac{16b^2(1 - \nu^2)F_c}{E_1 \pi^2 h} \quad ::$$

$$(\Delta L = 2b\epsilon) \text{ and } \left(\sigma_c = \frac{F_c}{h} = \left(\frac{\pi^2}{12} \right) \frac{E_1}{(1 - \nu^2)} \left(\frac{h}{b} \right)^2 \right)$$

$$\delta = \frac{4b}{\pi} \sqrt{\left[\epsilon - \frac{(1 - \nu^2)}{E_1} \right] \sigma_c}$$

$$\delta = \frac{4b}{\pi} \sqrt{\frac{(1 - \nu^2)}{E_1} (\sigma - \sigma_c)}$$

Appendix 2. Derivation of Equation (20)

$$\tan(\psi) = \frac{4 + \sqrt{3} \sqrt{\left[\left(\frac{4}{3} \right) \left(\frac{\sigma}{\sigma_c} - 1 \right) \right]} \tan \omega}{-4 \tan \omega + \sqrt{3} \sqrt{\left[\left(\frac{4}{3} \right) \left(\frac{\sigma}{\sigma_c} - 1 \right) \right]}} \quad :: \left(\text{combined with eq.; } \zeta = \sqrt{\frac{4}{3} \left(\frac{\sigma}{\sigma_c} - 1 \right)} \right)$$

$$\tan(\psi) = \frac{4 + \sqrt{4 \left(\frac{\sigma}{\sigma_c} - 1 \right)} \tan \omega}{-4 \tan \omega + \sqrt{4 \left(\frac{\sigma}{\sigma_c} - 1 \right)}}$$

$$\psi = \tan^{-1} \left[\frac{\left(4 + \sqrt{4 \left(\frac{\sigma}{\sigma_c} - 1 \right) \tan \omega} \right)}{-4 \tan \omega + \sqrt{4 \left(\frac{\sigma}{\sigma_c} - 1 \right)}} \right]$$

Appendix 3. Derivation of Equation (22)

$$\begin{aligned} \tan \psi \left[-4 \tan \omega + \sqrt{4 \left(\frac{\sigma}{\sigma_c} - 1 \right)} \right]^{\frac{1}{2}} &= 4 + \sqrt{4 \left(\frac{\sigma}{\sigma_c} - 1 \right)}^{\frac{1}{2}} \tan \omega \quad \because \\ &\left(\text{Refer eq.; } \psi = \tan^{-1} \left[\frac{\left(4 + \sqrt{4 \left(\frac{\sigma}{\sigma_c} - 1 \right) \tan \omega} \right)}{-4 \tan \omega + \sqrt{4 \left(\frac{\sigma}{\sigma_c} - 1 \right)}} \right] \right) \\ &- 4 [\tan \psi \tan \omega + 1] \\ &= \sqrt{4 \left(\frac{\sigma}{\sigma_c} - 1 \right)}^{\frac{1}{2}} [\tan \omega - \tan \psi] \end{aligned}$$

$$\begin{aligned} \sqrt{\frac{\sqrt{4} [\tan \psi \tan \omega + 1]}{\tan \psi - \tan \omega}} + 1 &= \frac{\sigma}{\sigma_c} \quad \because \\ &\left(\text{as per trigonometric formula } \frac{[\tan \psi \tan \omega + 1]}{\tan \psi - \tan \omega} = \frac{1}{\tan(\psi - \omega)} \right) \end{aligned}$$

$$\frac{\sigma}{\sigma_c} = \sqrt{\frac{2}{\tan(\psi - \omega)}} + 1$$

Appendix 4. Derivation of Equation (25)

$$\frac{G}{G_m} = \left(1 - \frac{\sigma_c}{\sigma} \right) \left(1 + \frac{3\sigma_c}{\sigma} \right)$$

$$\frac{G}{\Gamma(\psi)} = \frac{G}{\Gamma_{IC}f(\psi)} = \frac{G}{G_m f\left(\frac{\sigma_c}{\sigma}\right)} = 1 \quad \because \quad f\left(\frac{\sigma_c}{\sigma}\right) = 1 + 2\left(\frac{\sigma_c}{\sigma}\right) - 3\left(\frac{\sigma_c}{\sigma}\right)^2$$

$$f\left(\frac{\sigma_c}{\sigma}\right) = -3 \left(\frac{1}{\sqrt{\frac{2(1-\Upsilon)}{\tan(\psi(1-\lambda)-\omega)} + 1}} \right)^2 + 2 \left(\frac{1}{\sqrt{\frac{2(1-\Upsilon)}{\tan(\psi(1-\lambda)-\omega)} + 1}} \right) + 1 \quad \because$$

$$\left(\text{combined with eq.}; \frac{\sigma_c}{\sigma} = \frac{1}{\sqrt{\frac{2}{\tan(\psi-\omega)} + 1}} \right)$$